

# Upper-plate controls on co-seismic slip in the 2011 magnitude 9.0 Tohoku-oki earthquake

Dan Bassett<sup>1</sup>, David T. Sandwell<sup>1</sup>, Yuri Fialko<sup>1</sup> & Anthony B. Watts<sup>2</sup>

**The March 2011 Tohoku-oki earthquake was only the second giant (moment magnitude  $M_w \geq 9.0$ ) earthquake to occur in the last 50 years and is the most recent to be recorded using modern geophysical techniques. Available data place high-resolution constraints on the kinematics of earthquake rupture<sup>1</sup>, which have challenged prior knowledge about how much a fault can slip in a single earthquake and the seismic potential of a partially coupled megathrust interface<sup>2</sup>. But it is not clear what physical or structural characteristics controlled either the rupture extent or the amplitude of slip in this earthquake. Here we use residual topography and gravity anomalies to constrain the geological structure of the overthrusting (upper) plate offshore northeast Japan. These data reveal an abrupt southwest–northeast-striking boundary in upper-plate structure, across which gravity modelling indicates a south-to-north increase in the density of rocks overlying the megathrust of 150–200 kilograms per cubic metre. We suggest that this boundary represents the offshore continuation of the Median Tectonic Line, which onshore juxtaposes geological terranes composed of granite batholiths (in the north) and accretionary complexes (in the south)<sup>3</sup>. The megathrust north of the Median Tectonic Line is interseismically locked<sup>2</sup>, has a history of large earthquakes (18 with  $M_w > 7$  since 1896) and produced peak slip exceeding 40 metres in the Tohoku-oki earthquake<sup>1</sup>. In contrast, the megathrust south of this boundary has higher rates of interseismic creep<sup>2</sup>, has not generated an earthquake with  $M_J > 7$  (local magnitude estimated by the Japan Meteorological Agency) since 1923, and experienced relatively minor (if any) co-seismic slip in 2011<sup>1</sup>. We propose that the structure and frictional properties of the overthrusting plate control megathrust coupling and seismogenic behaviour in northeast Japan.**

The seismic moment of megathrust earthquakes is proportional to the product of rupture area, the average amount of slip, and the effective shear modulus<sup>4</sup>. Most variability is usually attributed to rupture area and so research has focused on the structural and geometrical barriers that segment plate boundaries and limit the dimensions, and thus magnitude, of earthquakes. Previous studies have shown the roughness of subducting plates to be one of the first-order controls on rupture dimensions<sup>5–7</sup>; but the amplitude of slip is proportional to the rupture area and the stress drop<sup>8</sup>, and may be harder to predict. In particular, of the five earthquakes since 1900 that had  $M_w \geq 9$ , the March 2011 Tohoku-oki earthquake had the smallest rupture area by 50% (that is, its rupture area was 0.5 that of the next-smallest earthquake in Kamchatka in 1952), but had the largest maximum displacements by 75% (that is, its maximum slip was 1.75 times that of the next-largest earthquake in Chile in 1960) (ref. 1 and Extended Data Fig. 1).

Geodetic observations show that most of the elastic strain energy released in megathrust earthquakes is accumulated in the overthrusting plate<sup>2</sup> so mapping along-strike variations in upper-plate structure is critical to understanding fault loading. But identifying upper-plate structural variations from the topography and gravity fields is difficult because the relatively small-amplitude, short-wavelength structure is

masked by the large-amplitude, trench-normal topography and gravity gradients associated with subduction zones. Here the application of spectral averaging routines designed to isolate and remove these gradients<sup>9,10</sup> provides observations that reveal how the crustal structure of the northeast Japan forearc influenced the rupture pattern of the Tohoku-oki earthquake.

Residual topography and gravity anomalies were calculated by regionally subtracting a spectral average of the trench-normal topography and gravity anomalies, and are shown in Fig. 1 (see Methods and Extended Data Fig. 2 for grid processing). The Pacific oceanic plate is subducting beneath Honshu at 80–85 mm yr<sup>-1</sup> and the submarine volcanoes of Erimo and the Joban seamounts are observed as positive residual topographic anomalies with amplitude >2 km both seaward and landward of the trench axis. The absence of similar anomalies along-strike suggests that the northeast Japan megathrust is relatively smooth. Across the forearc, our analysis reveals an abrupt and approximately linear transition in structure striking southwest–northeast (red dashed line in Fig. 1). Residual topography and gravity anomalies regionally increase from south to north across this boundary by ~0.8 km and ~60 mGal respectively (Fig. 1d). A second across-forearc transition of similar bathymetric character is located southeast of Hokkaido. The smooth and homogeneous nature of the subducting Pacific plate seaward of the trench axis strongly suggests that both transitions are related to the structure of the overthrusting plate.

Extension of the southern Japan forearc boundary to the trench axis makes it unlikely that variations in forearc Moho depth contribute to the along-strike contrast in gravity anomalies. We thus attribute residual gravity anomalies to trench-slope topography and lateral variations in the density of rocks comprising the overthrusting plate. The density contrasts associated with these variations are estimated by discretizing the forearc into 10 km × 10 km vertical prisms extending between the sea floor and the seismically constrained base of the forearc crust (Extended Data Figs 3–7), with a single density anomaly calculated for each prism (see Methods). The contrast in residual gravity anomalies can be explained by a south-to-north increase in the mean density of forearc rocks by ~150–200 kg m<sup>-3</sup> (Fig. 1c, d). The inverse proportionality between density contrasts and crustal thickness makes this a minimum estimate and the reduction in crustal thickness near the trench axis increases the magnitude of density contrasts (Fig. 1c). This analysis shows that the sharp change in trench-slope morphology is coincident with a transition in the density of the materials that comprise the southern Japan forearc crust.

The onshore geology<sup>11</sup> of Japan provides a physical interpretation of this transition (Fig. 2). The Median Tectonic Line (MTL) is the most prominent structural boundary and clearly separates two contrasting geological terrains. On the continent (north) side, a ~20-km-thick granitic upper-crust reflects intrusion of arc melt since the Cambrian Period<sup>3</sup>. In contrast, on the ocean (south) side, the forearc crust is entirely composed of variably metamorphosed Late Mesozoic to Cenozoic accretionary complexes<sup>3</sup>. A variety of tectonic models have been proposed to explain the unnatural juxtaposition of these terrains<sup>3</sup>,

<sup>1</sup>Scripps Institution of Oceanography, La Jolla, California 92093, USA. <sup>2</sup>Department of Earth Sciences, University of Oxford, South Parks Road, Oxford, UK.

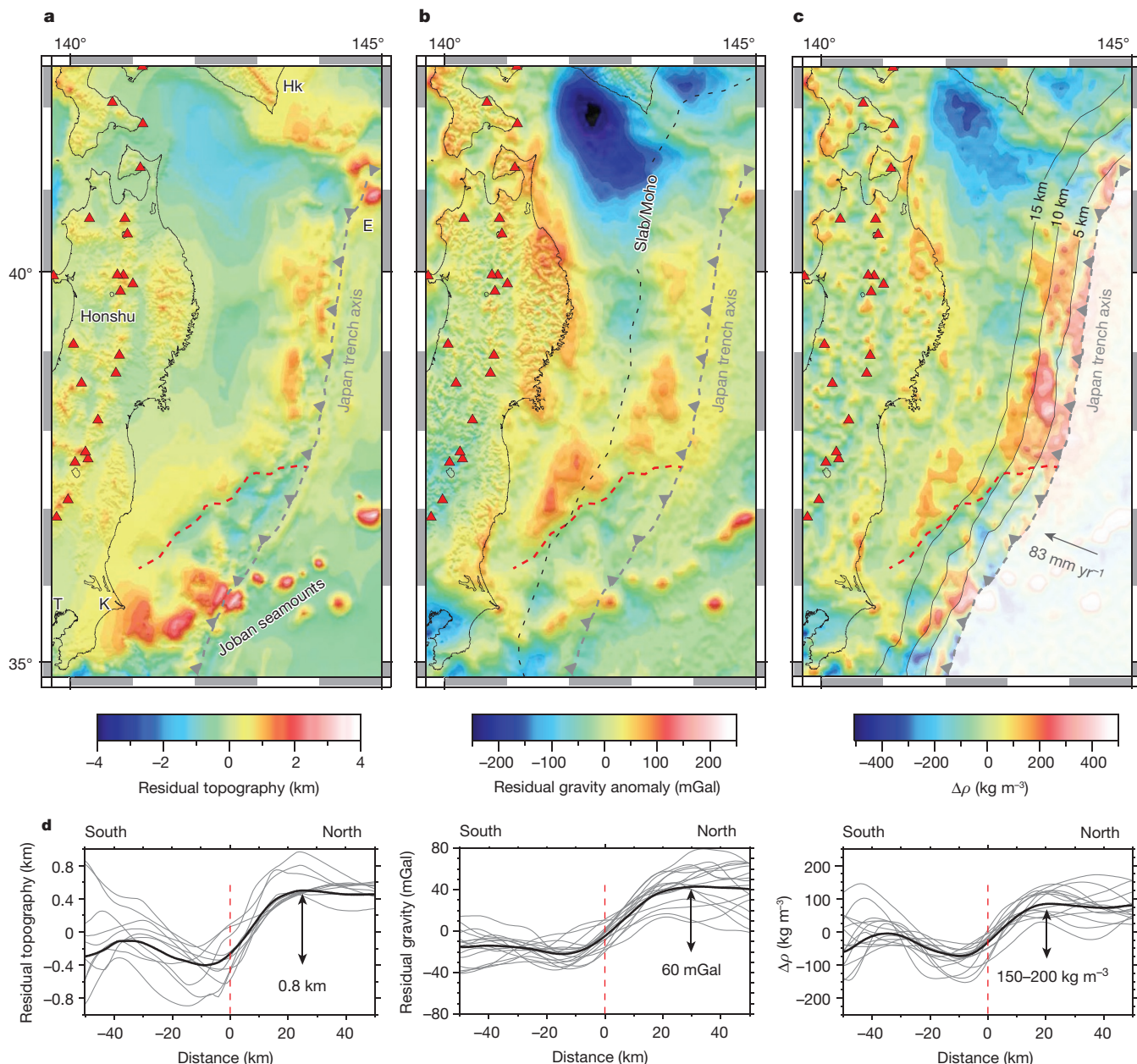


**Figure 1 | Forearc anomalies in the northeast Japan subduction zone.** **a**, Residual topography. Dashed red and grey lines mark the forearc segment boundary and the trench-axis respectively. Triangles show arc volcanoes. Hk, Hokkaido; E, Erimo seamount; T, Tokyo; K, Kashima. **b**, Residual gravity anomalies. The black dashed line marks the intersection of the subducting slab with the forearc Moho. **c**, Mean forearc density

anomalies. Contours (5-km increment) show forearc crustal thickness. **d**, Profiles (grey lines) perpendicularly traversing the forearc segment boundary showing the south-to-north increases in topography (~0.8 km), residual gravity anomaly (~60 mGal) and mean forearc density anomalies (~150–200 kg m<sup>-3</sup>). The mean for each ensemble of profiles is plotted in black.

but magnetotelluric<sup>12</sup> and active source seismic<sup>13,14</sup> data show a shallow (35°–45°) north-dipping fault geometry that is most consistent with a thrust faulting origin either along a low-angle mid-crustal detachment<sup>3</sup> or the Cretaceous subduction megathrust<sup>14</sup>. These data further demonstrate that the fundamental contrast in upper-plate structure expressed in surface geology across the MTL persists to depths of at least 20 km (ref. 13).

We propose that the MTL extends offshore Kashima, connecting to the step in residual gravity and bathymetry. The implication is that the abrupt change in forearc structure represents the lithological juxtaposition of granitic batholiths to the north and accretionary complexes to the south. This suggestion is consistent with the offshore extent of positive aeromagnetic anomalies, which have been modelled as batholiths 10–15 km thick<sup>15</sup>. The trend of aeromagnetic anomalies (red dashed line in Fig. 2) correlates the largest-amplitude residual gravity anomaly

(labelled KB) with the Early Cretaceous Kitakami batholith, which is exposed onshore in the Kitakami mountains (KM) (Fig. 2). The presence of low-to-mid-pressure metamorphic rocks within the southern region of the Abukuma highland (AH) is consistent with the MTL geometry inferred offshore.

The most interesting and important aspect of this forearc transition is that it is highly correlated with the seismogenic behaviour of the megathrust, as shown in Fig. 3. First, the forearc segment boundary is associated with a sharp north-to-south reduction in the number of intermediate-magnitude earthquakes (Fig. 3a). Second, historical rupture areas of large ( $M_{wJ} > 7.0$ ) megathrust earthquakes between 1896 and March 2011 (Supplementary Table 2) are similarly focused north of the proposed extension of the MTL (Fig. 3b); and the megathrust to the south, where the forearc is characterized by negative bathymetric and gravimetric anomalies, has not generated an earthquake with

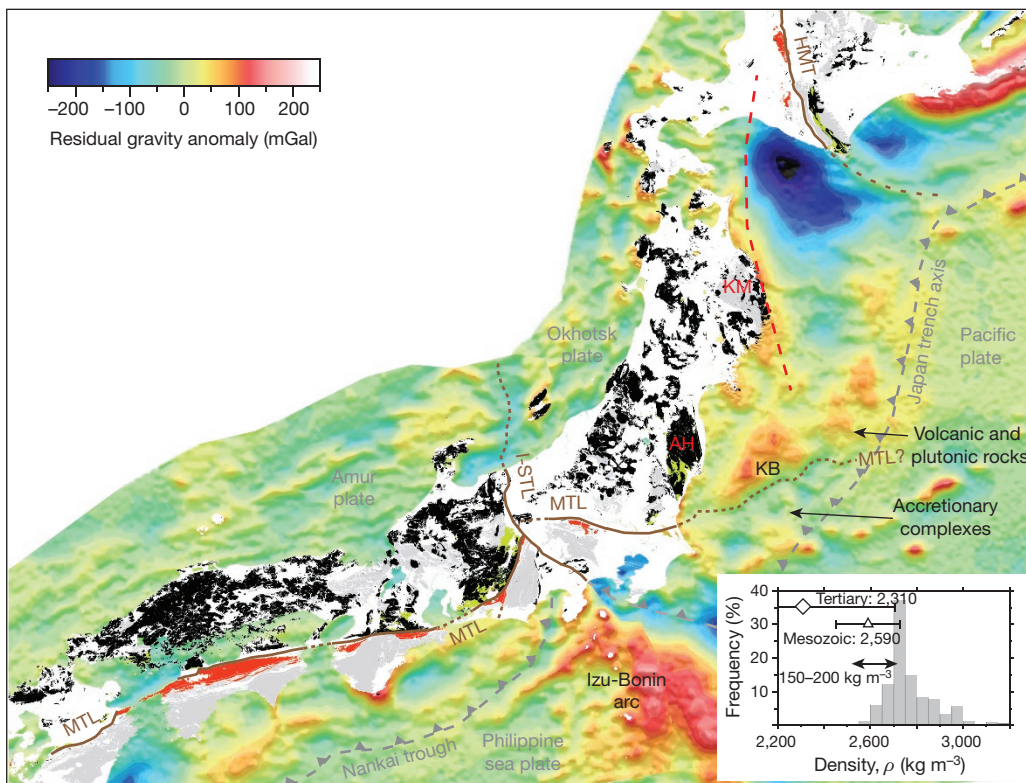


**Figure 2 | Simplified geology<sup>11</sup> and major tectonic boundaries<sup>3</sup> of Japan.** Volcanic and plutonic rocks (Cambrian to middle Miocene) are shown in black. Accretionary complexes (Jurassic to middle Miocene) are shown in grey. Metamorphic rocks (Cretaceous to middle Miocene) are shown in red and green. Main faults are shown in brown. MTL geometry is constrained by the juxtaposition of high-pressure footwall rocks (red shading indicates the Sanbagawa and Shimanto accretionary complexes) with coeval low-pressure granitic hanging-wall rocks (green shading indicates the Ryoke-Sanyo belt). Note the similar transition in peak metamorphic pressure observed across the Hidaka main thrust (HMT)

$M_I \geq 7.0$  in the >90-year duration of the Japan Meteorological Agency (<http://www.jma.go.jp/en/quake/>) earthquake catalogue. Third, there is a strong correlation between forearc structure and the distribution of co-seismic slip in the 2011  $M_w 9.0$  Tohoku-oki earthquake<sup>1</sup> (Fig. 3c). The Tohoku earthquake filled a seismic gap as defined by the rupture areas of earlier large thrust earthquakes (Fig. 3b) and most of the moment release occurred north of the forearc segment boundary in regions characterized by positive residual gravity anomalies. This correlation appears to be robust, as shown by a comparison with different published co-seismic slip models of the Tohoku earthquake that employed different data types and inversion algorithms (Extended Data Fig. 8). Finally, geodetically constrained interseismic deformation models all show a high degree of fault locking within the region of positive residual gravity<sup>2</sup>, but creep to the south of the forearc segment boundary (Fig. 3d, Supplementary Fig. 2).

The simplest interpretation of the relationships described above is that upper-plate lithology modulates the frictional behaviour of the megathrust. Frictional properties of typical crystalline rocks comprising the volcanic arc are characterized by a relatively high static coefficient of friction ( $\mu_0 = 0.6\text{--}0.8$ ) and strong velocity weakening<sup>16,17</sup>. Increasing clay content decreases the coefficient of friction ( $\mu_0 = 0.2\text{--}0.4$  in gouge with >50 wt% clay)<sup>16,18</sup> and promotes a more stable response to perturbations in fault slip rate<sup>18</sup>. Materials south of the forearc segment boundary are thus expected to be both weaker and less velocity weakening.

Numerical models of earthquake cycles incorporating rate- and state-dependent friction show that in the interseismic period, asperities are loaded at a rate modulated by their strength and location

in Hokkaido. KM, Kitakami mountains; KB, Kitakami batholith; AH, Abunuka highland; I-STL, Itoigawa-Shizuoka tectonic line. The strike of the Kitakami aeromagnetic anomalies is shown as a dashed red line<sup>15</sup>. The inset compares the density distribution of granitic rocks east of the volcanic arc in northeastern Honshu<sup>30</sup> and the mean dry densities for Tertiary and Mesozoic sedimentary rocks (error bars show one standard deviation)<sup>31</sup>. The modelled density contrast across the forearc segment boundary ( $\sim 150\text{--}200 \text{ kg m}^{-3}$ ) is within the range expected across the MTL.

relative to other asperities, and the flexural rigidity of the upper plate, which controls the extent of stress shadowing<sup>19,20</sup>. Stress increases are maximum on asperities with the highest  $\mu_0$  and the most negative values of the rate-dependent friction parameter  $a - b$ , relative to adjacent fault regions ( $a$  and  $b$  represent the magnitudes of the direct and evolution effect in friction respectively)<sup>21</sup>. Correspondingly, the stress drop and amplitude of co-seismic slip are amplified by sharper contrasts in frictional properties at the asperity boundaries<sup>22</sup>. Dynamic rupture simulations also show that dynamic rupture fronts decelerate as they penetrate into unloaded, velocity-strengthening, or compliant (less rigid) regions, which may ultimately arrest co-seismic ruptures<sup>23</sup>.

Under this framework, the anomalous nature of the Tohoku asperity may be attributed to the sharp transition in  $\mu_0$  and/or  $a - b$  across the MTL. The abrupt nature of this transition results in the local development of a large stress concentration in the interseismic period due to creep in (presumably) velocity-strengthening regions down-dip and south of the asperity. Low seismicity north and south of the asperity (Fig. 3a, b) may reflect reduced interseismic stressing rates within the Tohoku ‘stress shadow’. Simulations of earthquake cycles on a fault with heterogeneous distributions of  $\mu_0$  and  $a - b$  further reveal that large events can occur within the area that occasionally ruptures in great earthquakes (Extended Data Fig. 10). We propose that stress heterogeneities either side of the MTL may explain both the small slip area and the large slip amplitude of the Tohoku-oki earthquake rupture. (1) The extent of co-seismic slip was limited by the inability of the rupture front to penetrate into the low-stress or velocity-strengthening fault segment south of the MTL. (2) The highly stressed or strongly

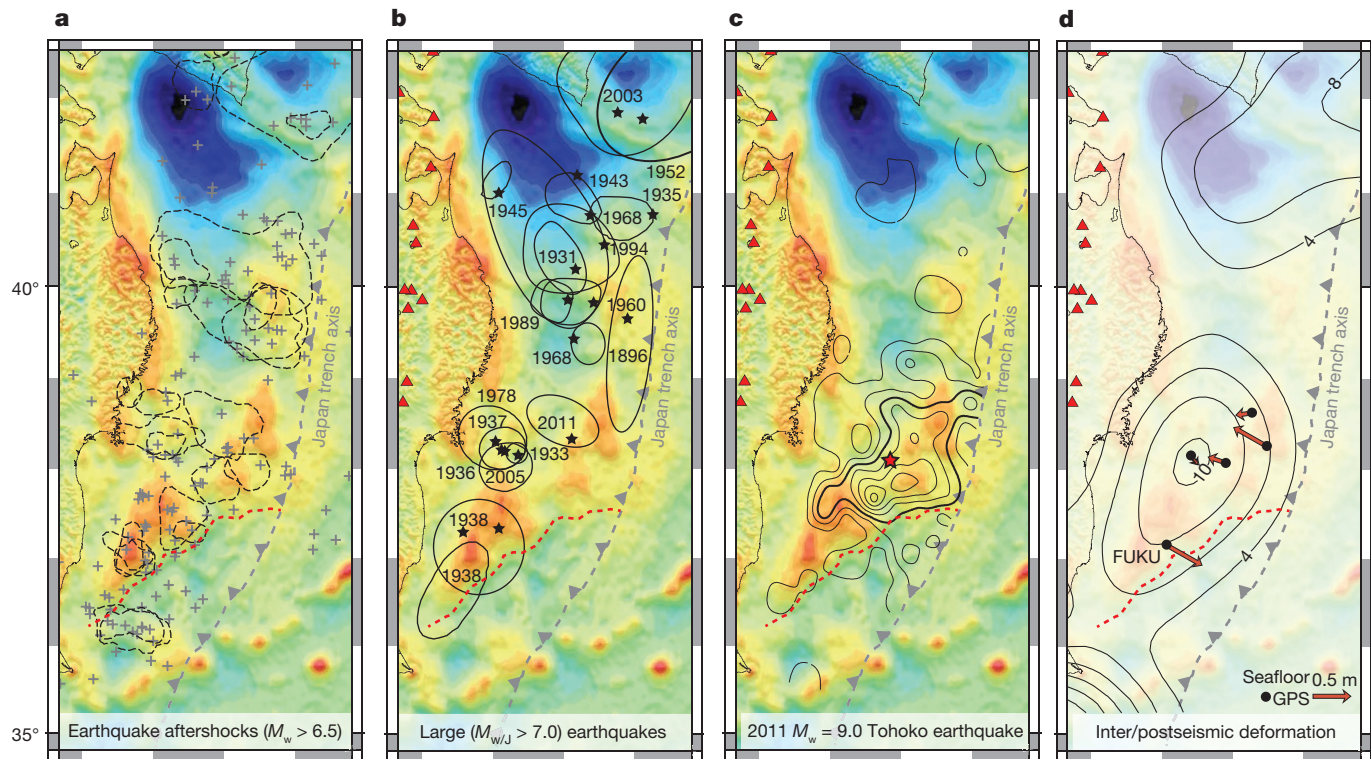


**Figure 3 | Slip behaviour of the northeast Japan megathrust.**

a, Instrumental earthquake record. Grey plus symbols show the epicentres of earthquakes in the JMA catalogue (1923–2015) with  $M_J \geq 6.5$ . Dashed ellipses show the aftershock area of thrust earthquakes in the Global Centroid Moment Tensor (<http://www.globalcmt.org>) catalogue (period 1976–2014) with  $6.5 \leq M_w < 8$ . No aftershock areas cross the forearc segment boundary (dashed red line). b, Rupture areas for large ( $M_{w/J} > 7.0$ ) megathrust earthquakes between 1896 and the 2011

velocity-weakening area with high rates of tectonic loading north of the MTL resulted in the large slip amplitude<sup>1</sup>. This interpretation implies accelerated postseismic afterslip within the ‘stress shadow’ areas of the Tohoku asperity. Robust afterslip has indeed been inferred in that area from the fast seaward motion of the seafloor Global Positioning System (GPS) site FUKU<sup>24</sup> (Fig. 3d and Extended Data Fig. 9). The seaward motion of this site is contrary to the postseismic landward motions observed at seafloor GPS sites within the main rupture area, and is probably caused by substantial afterslip south of the forearc segment boundary<sup>24</sup>. Regional seafloor geodetic measurements from a cabled seismological and geodetic observatory<sup>25</sup> will place important constraints on the extent of post-seismic creep and moment accumulation rates, and provide further insights into tectonic loading of the Tohoku asperity, fault-slip behaviour south of the MTL and, ultimately, seismic hazard in Kashima and eastern Tokyo.

The correlation between the forearc segment boundary and megathrust slip behaviour appears to persist west of the intersection between the slab with the forearc Moho. This may reflect subduction of eroded upper-plate materials beyond the forearc Moho, thereby extending the influence of upper-plate lithology on the frictional properties of the megathrust to greater depth. The obliquity of the MTL may cause subduction of eroded materials to reduce the along-strike gradient in frictional properties, but both the location and magnitude of this effect will depend on the depth range of tectonic erosion. Finally, the contrast in mean forearc density and trench-slope topography across the MTL will result in an along-strike variation in lithostatic pressure of 40–60 MPa. Although considerably lower than dip-parallel variations in lithostatic stress associated with slab-dip and trench-slope topography, dip-parallel lithostatic gradients occur both north and south of the MTL and the along-strike contrast in lithostatic

Tohoku-oki earthquake (Supplementary Table 3). c, Coseismic slip contours (10-m increment) for the 2011  $M_w$  9 Tohoku-oki earthquake<sup>1</sup>. The 20-m slip contour (thicker contour line) defines the Tohoku asperity. d, Inter/postseismic deformation. Contours show interseismic back-slip rate (increment  $2 \text{ cm yr}^{-1}$ )<sup>2</sup>. Arrows show 1-year postseismic displacements of seafloor GPS sites<sup>24</sup>. The fast seaward motion of site FUKU is associated with shallow afterslip<sup>24</sup>.

stress may still be important in influencing the lateral distribution of plate locking at a given depth.

Two additional insights from this study may be important for understanding seismic hazard in other subduction zones. The first comes from the observation that the accreted terranes that appear to be creeping south of the forearc segment boundary<sup>2</sup> also overlie the Nankai megathrust in southwest Japan, which is characterized by interseismic locking<sup>26</sup> and produced large earthquakes in 1944 ( $M_w$  8.1), 1946 ( $M_w$  8.3) and 1968 ( $M_w$  7.5)<sup>27</sup>. On one hand, this may reflect differences in the relative proportion of subducting and overthrusting plate materials within the megathrust shear zone, and the strong dependence of the  $a - b$  value of clay-rich sediments on lithologic heterogeneity<sup>28</sup>. On the other hand, the amplitude of stress heterogeneities is dependent on spatial gradients in  $\mu_0$  and  $a - b$ . The apparent low seismicity north and south of the Tohoku asperity might be due to ‘stress shadowing’, resulting in interseismic stressing rates on the megathrust even lower than those implied by models of interseismic coupling (Fig. 3d). In Nankai, the composition of the overthrusting plate is more homogeneous along-strike, which may result in smaller variations in fault frictional properties, and more uniform interseismic loading rates. These factors are likely to encourage earthquake ruptures in Nankai to extend over larger areas. The second insight is that low residual gravity anomalies are not a good indicator of seismogenic behaviour, as proposed in previous studies<sup>27,29</sup>. The residual topography and gravity fields are now available for all subduction zones on Earth<sup>9,10</sup>, but their real utility comes from enabling existing and future seismological and geodetic observations to be considered in the context of subducting and overthrusting plate structure. This study shows that these considerations are an essential component of hazard assessment.

**Online Content** Methods, along with any additional Extended Data display items and Source Data, are available in the online version of the paper; references unique to these sections appear only in the online paper.

Received 26 June; accepted 11 December 2015.

1. Minson, S. et al. Bayesian inversion for finite fault earthquake source models—II: the 2011 great Tohoku-oki, Japan earthquake. *Geophys. J. Int.* **198**, 922–940 (2014).
2. Suwa, Y., Miura, S., Hasegawa, A., Sato, T. & Tachibana, K. Interplate coupling beneath NE Japan inferred from three-dimensional displacement field. *J. Geophys. Res.* **111**, B04402 (2006).
3. Isozaki, Y., Aoki, K., Nakama, T. & Yanai, S. New insight into a subduction-related orogen: a reappraisal of the geotectonic framework and evolution of the Japanese Islands. *Gondwana Res.* **18**, 82–105 (2010).
4. Aki, K. Estimation of earthquake moment, released energy, and stress-strain drop from G-wave spectrum. *Bull. Earthq. Res. Inst.* **44**, 23–88 (1966).
5. Wang, K. & Bilek, S. L. Fault creep caused by subduction of rough seafloor relief. *Tectonophysics* **610**, 1–24 (2014).
6. Robinson, D. P., Das, S. & Watts, A. B. Earthquake rupture stalled by a subducting fracture zone. *Science* **312**, 1203–1205 (2006).
7. Sparkes, R., Tilmann, F., Hovius, N. & Hillier, J. Subducted seafloor relief stops rupture in South American great earthquakes: implications for rupture behaviour in the 2010 Maule, Chile earthquake. *Earth Planet. Sci. Lett.* **298**, 89–94 (2010).
8. Knopoff, L. Energy release in earthquakes. *Geophys. J. Int.* **1**, 44–52 (1958).
9. Bassett, D. & Watts, A. B. Gravity anomalies, crustal structure, and seismicity at subduction zones: 1. Seafloor roughness and subducting relief. *Geochem. Geophys. Geosyst.* **16**, 1508–1540 (2015).
10. Bassett, D. & Watts, A. B. Gravity anomalies, crustal structure, and seismicity at subduction zones: 2. Interrelationships between fore-arc structure and seismogenic behavior. *Geochem. Geophys. Geosyst.* **16**, 1541–1576 (2015).
11. Seamless Digital Geological Map of Japan 1: 200,000. Jul 3, 2012 version, Research Information Database DB084 ([https://gbank.gsj.jp/seamless/index\\_en.html?](https://gbank.gsj.jp/seamless/index_en.html?)), Geological Survey of Japan, National Institute of Advanced Industrial Science and Technology (2012).
12. Goto, T., Yamaguchi, S., Sumitomo, N. & Yaskawa, K. The electrical structure across the Median Tectonic Line in east Shikoku, southwest Japan. *Earth Planets Space* **50**, 405–415 (1998).
13. Kawamura, T., Onishi, M., Kurashimo, E., Ikawa, T. & Ito, T. Deep seismic reflection experiment using a dense receiver and sparse shot technique for imaging the deep structure of the Median Tectonic Line (MTL) in east Shikoku, Japan. *Earth Planets Space* **55**, 549–557 (2003).
14. Sato, H., Kato, N., Abe, S., Van Horne, A. & Takeda, T. Reactivation of an old plate interface as a strike-slip fault in a slip-partitioned system: Median Tectonic Line, SW Japan. *Tectonophysics* **644**, 58–67 (2015).
15. Finn, C. Aeromagnetic evidence for a buried Early Cretaceous magmatic arc, northeast Japan. *J. Geophys. Res.* **99**, 22165–22185 (1994).
16. Morrow, C., Moore, D. E. & Lockner, D. The effect of mineral bond strength and adsorbed water on fault gouge frictional strength. *Geophys. Res. Lett.* **27**, 815–818 (2000).
17. Mitchell, E., Fialko, Y. & Brown, K. Temperature dependence of frictional healing of Westerly granite: experimental observations and numerical simulations. *Geochem. Geophys. Geosyst.* **14**, 567–582 (2013).
18. Numelin, T., Marone, C. & Kirby, E. Frictional properties of natural fault gouge from a low-angle normal fault, Panamint Valley, California. *Tectonics* **26** (2), 1–14 (2007).
19. Kanamori, H. The nature of seismicity patterns before large earthquakes. *Earthquake Prediction* **4**, 1–19 (1981).
20. Hetland, E. & Simons, M. Post-seismic and interseismic fault creep. II: Transient creep and interseismic stress shadows on megathrusts. *Geophys. J. Int.* **181**, 99–112 (2010).
21. Kaneko, Y., Avouac, J.-P. & Lapusta, N. Towards inferring earthquake patterns from geodetic observations of interseismic coupling. *Nature Geosci.* **3**, 363–369 (2010).
22. Hillers, G. & Wesnousky, S. Scaling relations of strike-slip earthquakes with different slip-rate-dependent properties at depth. *Bull. Seismol. Soc. Am.* **98**, 1085–1101 (2008).
23. Tinti, E., Bazzarri, A. & Cocco, M. Modeling the dynamic rupture propagation on heterogeneous faults with rate-and state-dependent friction. *Ann. Geophys.* **48** (2), 327–345 (2005).
24. Sun, T. & Wang, K. Viscoelastic relaxation following subduction earthquakes and its effects on afterslip determination. *J. Geophys. Res.* **120**, 1329–1344 (2015).
25. Kanazawa, T. in *Underwater Technology Symposium IEEE International 1–5*, <http://dx.doi.org/10.1109/UT.2013.6519911> (IEEE, 2013).
26. Wallace, L. M. et al. Enigmatic, highly active left-lateral shear zone in southwest Japan explained by aseismic ridge collision. *Geology* **37**, 143–146 (2009).
27. Wells, R. E., Blakely, R. J., Sugiyama, Y., Scholl, D. W. & Dinterman, P. A. Basin-centered asperities in great subduction zone earthquakes: a link between slip, subsidence, and subduction erosion? *J. Geophys. Res.* **108** (B10), 1–30 (2003).
28. den Hartog, S., Niemeijer, A. & Spiers, C. New constraints on megathrust slip stability under subduction zone P-T conditions. *Earth Planet. Sci. Lett.* **353/354**, 240–252 (2012).
29. Song, T. & Simons, M. Large trench-parallel gravity variations predict seismogenic behavior in subduction zones. *Science* **301**, 630–633 (2003).
30. Okuma, S. & Kanaya, H. Petrophysical Data Base of Basement Rocks in Japan for the 21st Century (PB-Rock 21). RIO-DB (Research Information Data Base) **87**, <http://riodb02.ibase.aist.go.jp/pb-rock21/index.html> (Geological Survey of Japan, AIST, 2011).
31. Murata, Y., Suda, Y., Kikuchi, T. & Chōsajo, C. *Rock Physical Properties of Japan: Density, Magnetism, P-Wave Velocity, Porosity, Thermal Conductivity* (Geological Survey of Japan, 1991).

**Supplementary Information** is available in the online version of the paper.

**Acknowledgements** We thank S. Naif, C. Davies, C. Twardzik and S. Das for suggestions. Figures and grid processing was conducted using the Generic Mapping Tools (GMT) (<http://gmt.soest.hawaii.edu/>). D.B. was supported by a University of Oxford Clarendon Scholarship, by a Green Foundation Postdoctoral Fellowship in the Institute of Geophysics and Planetary Physics, Scripps Institution of Oceanography, University of California, San Diego, by the National Geospatial Agency (HM01771310008), and by the Scripps Seafloor Electromagnetics Consortium (<http://marineemlab.ucsd.edu/semc.html>).

**Author Contributions** D.B. and A.B.W. conceived the study and conducted grid processing. D.B. and D.T.S. calculated density anomalies. Y.F. conducted numerical simulations of earthquake cycles. D.B., D.T.S. and Y.F. wrote the initial manuscript. All authors discussed the results and commented on the manuscript.

**Author Information** Reprints and permissions information is available at [www.nature.com/reprints](http://www.nature.com/reprints). The authors declare no competing financial interests. Readers are welcome to comment on the online version of the paper. Correspondence and requests for materials should be addressed to D.B. (dbassett@ucsd.edu).

## METHODS

**Spectral averaging of topography and gravity grids.** Residual anomalies are calculated using the satellite-derived free-air gravity anomaly grid of Sandwell *et al.*<sup>32</sup> and the GEBCO shipboard bathymetry grid<sup>33</sup>. Free-air gravity anomalies onshore are reduced to Bouguer gravity anomalies using a crustal density of 2,670 kg m<sup>-3</sup>. Bathymetry and gravity grids are sampled by 1,200-km-long trench-normal profiles, which are centred on the bathymetrically defined trench-axis and spaced ~25 km along strike. The mean cross-sectional structure of the subduction zone is calculated as the spectral average across each ensemble of profiles. The linearity of the fast Fourier transform and its inverse means that spectral averages should be indistinguishable from arithmetic averages, but small differences ( $\leq 10$  m and  $\leq 2$  mGal) are present, resulting from the finite precision of the fast Fourier transform and associated down-sampling<sup>9</sup>. Maintaining the geometry of the trench axis, average profiles are extended along-strike to produce grids of each ensemble average profile, which is then subtracted from the original data set to produce grids of residual topography and residual gravity anomalies. In contrast to profile-based residual calculations, subtraction of an ensemble average grid preserves the full 1 min  $\times$  1 min resolution of the original data sets. This processing methodology has been applied globally<sup>9,10</sup> and is illustrated in Extended Data Fig. 2.

**Calculation of density anomalies.** Using the average topographic profile and active-source seismic constraints on across-arc crustal structure (Supplementary Table 2 and Extended Data Figs 4 and 5), the ensemble average gravity anomaly profile can be well fitted using realistic density distributions for the crust (~2,800 kg m<sup>-3</sup>) and mantle (~3,100 kg m<sup>-3</sup>) (Extended Data Fig. 3). This shows that the ensemble average gravity anomaly captures the broad crustal architecture of the subduction zone, enabling short-wavelength residual gravity anomalies landward of the trench axis to be interpreted as reflecting crustal structure of the forearc, arc and backarc.

The forearc segment boundary extends to the trench axis with no change in amplitude across the intersection of the subducting Pacific plate with the forearc Mohorovičić boundary (Moho) (Fig. 1b). It is thus unlikely (and nearer the trench impossible) that variations in forearc Moho depth contribute to the along-strike contrast in gravity anomalies. Hence, we attribute residual gravity anomalies to trench-slope topography and lateral changes in density of the overthrusting forearc crust. The magnitude of these changes are calculated by discretizing the forearc into 10 km  $\times$  10 km vertical prisms. The top of each prism is constrained by the sea floor and the base is constrained by either the forearc Moho or the top of the subducting slab (whichever is shallower). The geometry of both interfaces is constrained by active-source wide-angle seismic models (Extended Data Figs 4 and 5 and Supplementary Table 2). The initial density contrast  $\Delta\rho$  for each prism is calculated directly from the amplitude of residual gravity anomalies  $R_{\text{grav}}$ :

$$\Delta\rho = \frac{R_{\text{grav}}}{2\pi Gh}$$

where  $h$  is the crustal thickness of the forearc and  $G$  is the gravitational constant. Synthetic gravity anomalies are calculated using the *Fatiando:Gravmag* module<sup>34</sup>, which calculates the gravity effect of three-dimensional rectangular prisms using the formula of Plouff<sup>35</sup>. Outstanding residual gravity anomalies are used to update  $\Delta\rho$  within each prism. After 12 iterations the root-mean-square misfit between the observed and calculated residual gravity anomalies is  $< 1$  mGal (inset to Extended Data Fig. 6b). The magnitude of density contrasts is inversely proportional to the vertical extent of the causative prism. Our methodology thus yields minimum estimates with density contrasts distributed throughout the full thickness of the forearc crust,  $h$ . As shown by the contours in Fig. 1c, the larger density contrasts near the trench axis predominantly reflect the reduction in forearc crustal thickness (Extended Data Fig. 3c) although they may also reflect, in part, contrasting resistances to near-trench deformation. The distribution of density anomalies is not strongly dependent on the observations used to constrain forearc crustal thickness and experimentation between passive (SLAB1.0<sup>36</sup> and earthquake tomographic<sup>37</sup>) versus active-source seismic (Supplementary Table 2) constraints on subducting slab and forearc Moho geometries yield differences in density anomalies of  $< 10$  kg m<sup>-3</sup> (Extended Data Fig. 7). These differences are an order of magnitude smaller than the  $\sim 150$  kg m<sup>-3</sup> contrast in mean forearc density calculated across the forearc segment boundary (Fig. 1c-d).

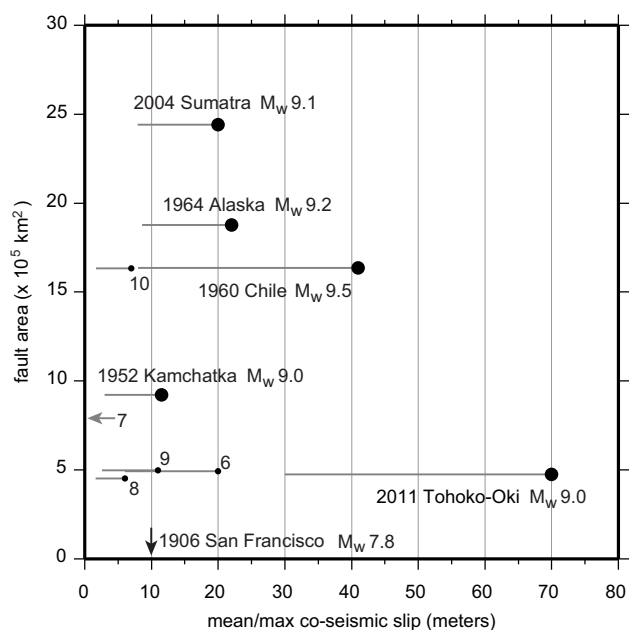
**Comparison with earthquake distributions.** Forearc structure is compared with the slip behaviour of the megathrust using published slip models and aftershock distributions for earthquakes with  $M_{\text{WJ}} > 7$  occurring since 1896. This catalogue is presented as Supplementary Table 3. For earthquakes with  $6.5 \leq M_{\text{w}} \leq 7.5$  between 1976 and 2015 (duration of instrumental records), rupture areas are estimated from the distribution of aftershocks in the International Seismological Center (ISC) (<http://www.isc.ac.uk/>) earthquake catalogue. Global analyses have shown that

there is little change in aftershock areas after the first week<sup>38</sup>, and we estimate rupture areas from one-week aftershock distributions.

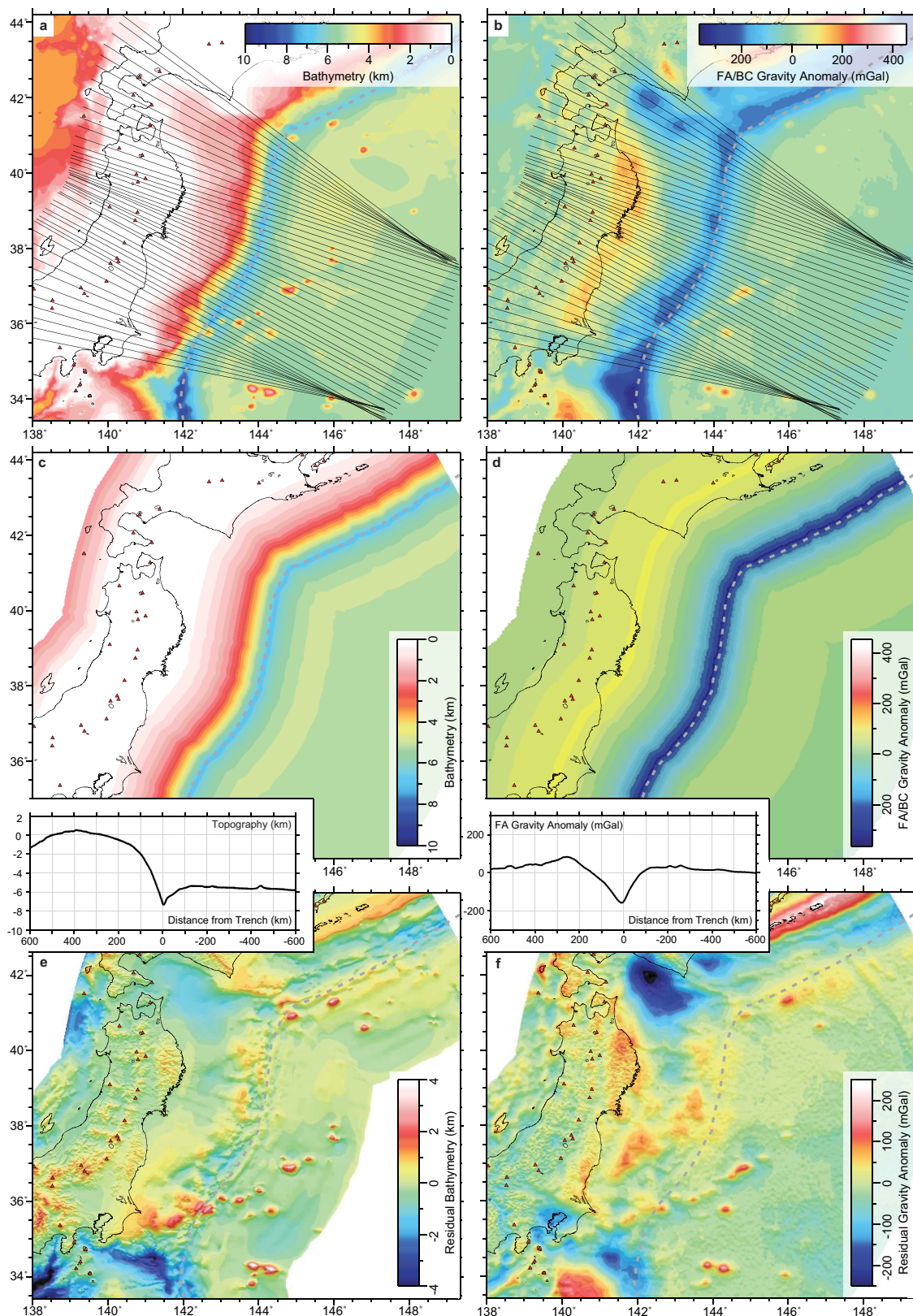
Tajima *et al.*<sup>39</sup> reviewed 44 published slip distributions for the Tohoku-oki earthquake. Most show the maximum slip to be  $\geq 40$  m. Following the asperity definition applied in northeast Japan by Yamanaka and Kikuchi<sup>40</sup>, we define the Tohoku asperity as regions where the co-seismic slip was  $\geq 20$  m and half the maximum slip amplitude (thickened contour Fig. 3c).

32. Sandwell, D. T., Müller, D. T., Smith, W. H. F., Garcia, E. & Francis, R. New global marine gravity from CryoSat-2 and Jason-1 reveals buried tectonic structure. *Science* **346**, 65–67 (2014).
33. Intergovernmental Oceanographic Commission, International Hydrographic Organisation, and British Oceanographic Data Centre. *Centenary Edition of the GEBCO Digital Atlas [CD-ROM]* ([http://www.gebco.net/data\\_and\\_products/girded\\_bathymetry\\_data/gebco\\_one\\_minute\\_grid/](http://www.gebco.net/data_and_products/girded_bathymetry_data/gebco_one_minute_grid/)) (British Oceanographic Data Centre, 2003).
34. Uieda, L., Oliveira, V. C., Jr & Barbosa, V. C. Modeling the Earth with Fatiando a Terra. *Proc. 12th ‘Python in Science’ Conf.* 96–103, <http://www.fatiando.org> (2013).
35. Plouff, D. Gravity and magnetic fields of polygonal prisms and application to magnetic terrain corrections. *Geophysics* **41**, 727–741 (1976).
36. Hayes, G. P., Wald, D. J. & Johnson, R. L. Slab1.0: a three-dimensional model of global subduction zone geometries. *J. Geophys. Res.* **117**, 1–15 (2012).
37. Katsumata, A. Depth of the Moho discontinuity beneath the Japanese islands estimated by travelttime analysis. *J. Geophys. Res.* **115**, 1–17 (2010).
38. Henry, C. & Das, S. Aftershock zones of large shallow earthquakes: fault dimensions, aftershock area expansion and scaling relations. *Geophys. J. Int.* **147**, 272–293 (2001).
39. Tajima, F., Mori, J. & Kennett, B. L. A review of the 2011 Tohoku-Oki earthquake (Mw 9.0): large-scale rupture across heterogeneous plate coupling. *Tectonophysics* **586**, 15–34 (2013).
40. Yamanaka, Y. & Kikuchi, M. Asperity map along the subduction zone in northeastern Japan inferred from regional seismic data. *J. Geophys. Res.* **109**, 1–16 (2004).
41. Barrientos, S. E. & Ward, S. N. The 1960 Chile earthquake: inversion for slip distribution from surface deformation. *Geophys. J. Int.* **103**, 589–598 (1990).
42. Johnson, J. M., Satake, K., Holdahl, S. R. & Sauber, J. The 1964 Prince William Sound earthquake: joint inversion of tsunami and geodetic data. *J. Geophys. Res.* **101**, 523–532 (1996).
43. Chlieh, M. *et al.* Coseismic slip and afterslip of the great Mw 9.15 Sumatra-Andaman earthquake of 2004. *Bull. Seismol. Soc. Am.* **97**, S152–S173 (2007).
44. Johnson, J. M. & Satake, K. in *Seismogenic and Tsunamigenic Processes in Shallow Subduction Zones* 541–553 (Springer, 1999).
45. Delouis, B., Nocquet, J. M. & Vallée, M. Slip distribution of the February 27, 2010 Mw= 8.8 Maule earthquake, central Chile, from static and high-rate GPS, InSAR, and broadband teleseismic data. *Geophys. Res. Lett.* **37**, 1–7 (2010).
46. Kelleher, J., Savino, J., Rowlett, H. & McCann, W. Why and where great thrust earthquakes occur along island arcs. *J. Geophys. Res.* **79**, 4889–4899 (1974).
47. Beck, S. L. & Christensen, D. H. Rupture process of the February 4, 1965, Rat Islands earthquake. *J. Geophys. Res.* **96**, 2205–2221 (1991).
48. Johnson, J. M. *et al.* The 1957 great Aleutian earthquake. *Pure Appl. Geophys.* **142**, 3–28 (1994).
49. Ito, A. *et al.* Fault plane geometry in the source region of the 1994 Sanriku-oki earthquake. *Earth Planets Sci. Lett.* **223**, 163–175 (2004).
50. Takahashi, N. *et al.* Seismic structure and seismogenesis off Sanriku region, northeastern Japan. *Geophys. J. Int.* **159**, 129–145 (2004).
51. Miura, S. *et al.* Structural characteristics off Miyagi forearc region, the Japan Trench seismogenic zone, deduced from a wide-angle reflection and refraction study. *Tectonophysics* **407**, 165–188 (2005).
52. Ito, A. *et al.* Bending of the subducting oceanic plate and its implication for rupture propagation of large interplate earthquakes off Miyagi, Japan, in the Japan Trench subduction zone. *Geophys. Res. Lett.* **32**, 1–4 (2005).
53. Miura, S. *et al.* Structural characteristics controlling the seismicity crustal structure of southern Japan Trench fore-arc region, revealed by ocean bottom seismographic data. *Tectonophysics* **363**, 79–102 (2003).
54. Fujie, G. *et al.* Along-trench structural variation and seismic coupling in the northern Japan subduction zone. *Earth Planets Space* **65**, 75–83 (2013).
55. Yamamoto, Y., Hino, R. & Shinohara, M. Mantle wedge structure in the Miyagi Prefecture forearc region, central northeastern Japan arc, and its relation to corner-flow pattern and interplate coupling. *J. Geophys. Res.* **116**, 1–18 (2011).
56. Fujie, G. *et al.* A significant relation between seismic activities and reflection intensities in the Japan Trench region. *Geophys. Res. Lett.* **29**, 1–4 (2002).
57. Wang, Z. & Zhao, D. Seismic imaging of the entire arc of Tohoku and Hokkaido in Japan using P-wave, S-wave and SP depth-phase data. *Phys. Earth Planet. Inter.* **152**, 144–162 (2005).
58. Simons, M. *et al.* The 2011 magnitude 9.0 Tohoku-Oki earthquake: mosaicking the megathrust from seconds to centuries. *Science* **332**, 1421–1425 (2011).
59. Ammon, C. J., Lay, T., Kanamori, H. & Cleveland, M. A rupture model of the 2011 off the Pacific coast of Tohoku earthquake. *Earth Planets Space* **63**, 693–696 (2011).
60. Yue, H. & Lay, T. Inversion of high-rate (1 sps) GPS data for rupture process of the 11 March 2011 Tohoku earthquake (Mw 9.1). *Geophys. Res. Lett.* **38**, 1–6 (2011).

61. Melgar, D. & Bock, Y. Kinematic earthquake source inversion and tsunami inundation prediction with regional geophysical data. *J. Geophys. Res.* **120**, 3324–3349 (2015).
62. Sato, T., Hiratsuka, S. & Mori, J. Precursory seismic activity surrounding the high-slip patches of the 2011 Mw 9.0 Tohoku-Oki earthquake. *Bull. Seismol. Soc. Am.* **103**, 3104–3114 (2013).
63. Ozawa, S. *et al.* Preceding, coseismic, and postseismic slips of the 2011 Tohoku earthquake, Japan. *J. Geophys. Res.* **117**, 1–20 (2012).
64. Fujii, Y. & Satake, K., Sakai, S. i., Shinohara, M. & Kanazawa, T. Tsunami source of the 2011 off the Pacific coast of Tohoku Earthquake. *Earth Planets Space* **63**, 815–820 (2011).
65. Asano, Y. *et al.* Spatial distribution and focal mechanisms of aftershocks of the 2011 off the Pacific coast of Tohoku Earthquake. *Earth Planets Space* **63**, 669–673 (2011).
66. Lapusta, N. & Rice, J. R., Ben-Zion, Y. & Zheng, G. Elastodynamic analysis for slow tectonic loading with spontaneous rupture episodes on faults with rate-and state-dependent friction. *J. Geophys. Res.* **105**, 23765–23789 (2000).
67. Kaneko, Y., Fialko, Y., Sandwell, D., Tong, X. & Furuya, M. Interseismic deformation and creep along the central section of the North Anatolian fault (Turkey): InSAR observations and implications for rate-and-state friction properties. *J. Geophys. Res.* **118**, 316–331 (2013).

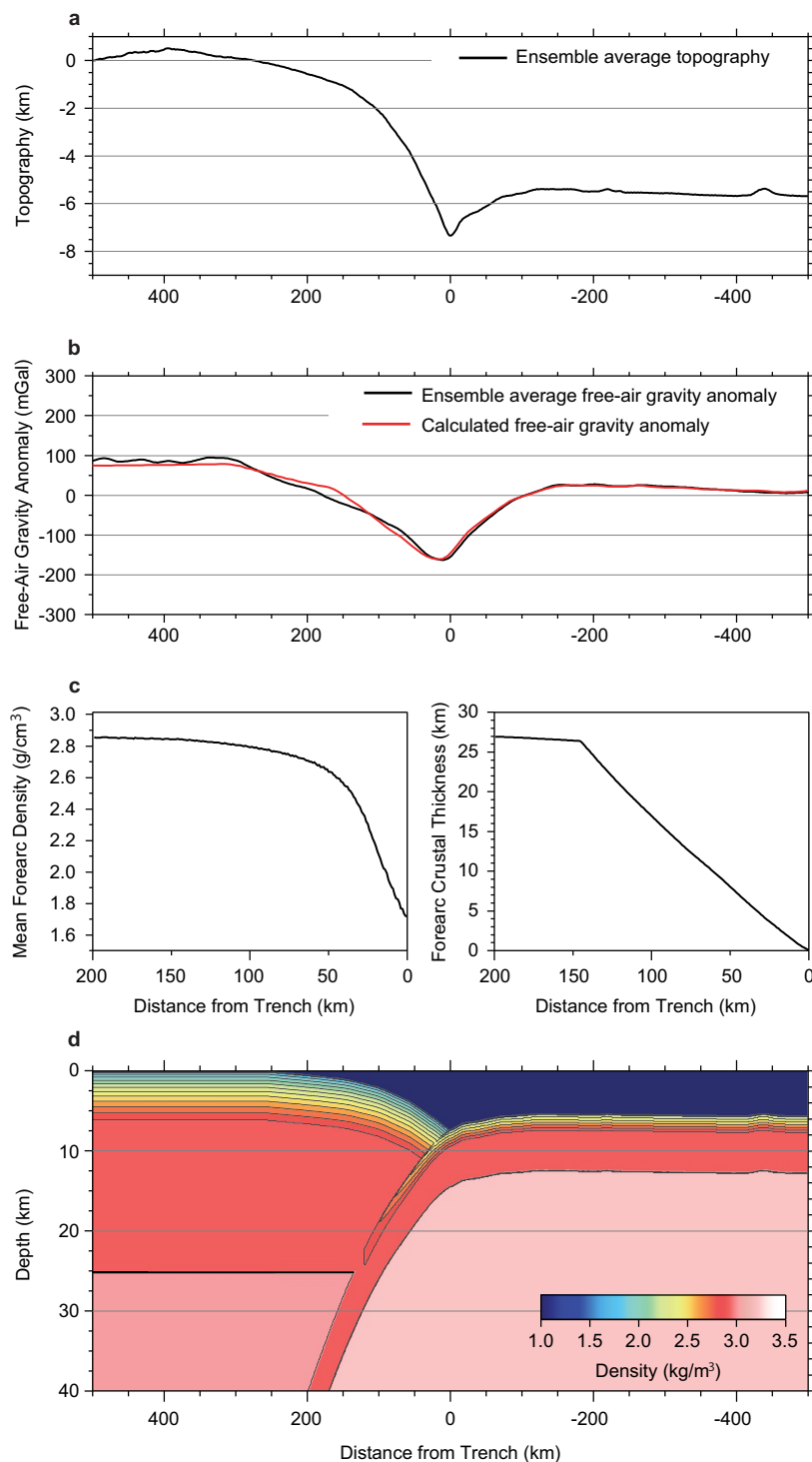


**Extended Data Figure 1 | Rupture areas and co-seismic slip amplitudes in Earth's largest earthquakes<sup>1,41–48</sup>.** Grey bars and black dots plot the mean and maximum amounts of co-seismic slip against the area of fault rupture. The five earthquakes with  $M_w \geq 9$  are labelled and numbers 6–10 refer to the location of smaller-magnitude earthquakes in the catalogue shown in Supplementary Table 1. Note the anomalously large (>70 m) amount of co-seismic slip in the 2011 Tohoku-oki event<sup>1</sup>. The black arrow shows the maximum amount of slip in the 1906 San Francisco earthquake. The rupture area in this strike-slip event was  $6 \times 10^3 \text{ km}^2$  and two orders of magnitude smaller than the megathrust rupture areas plotted here.



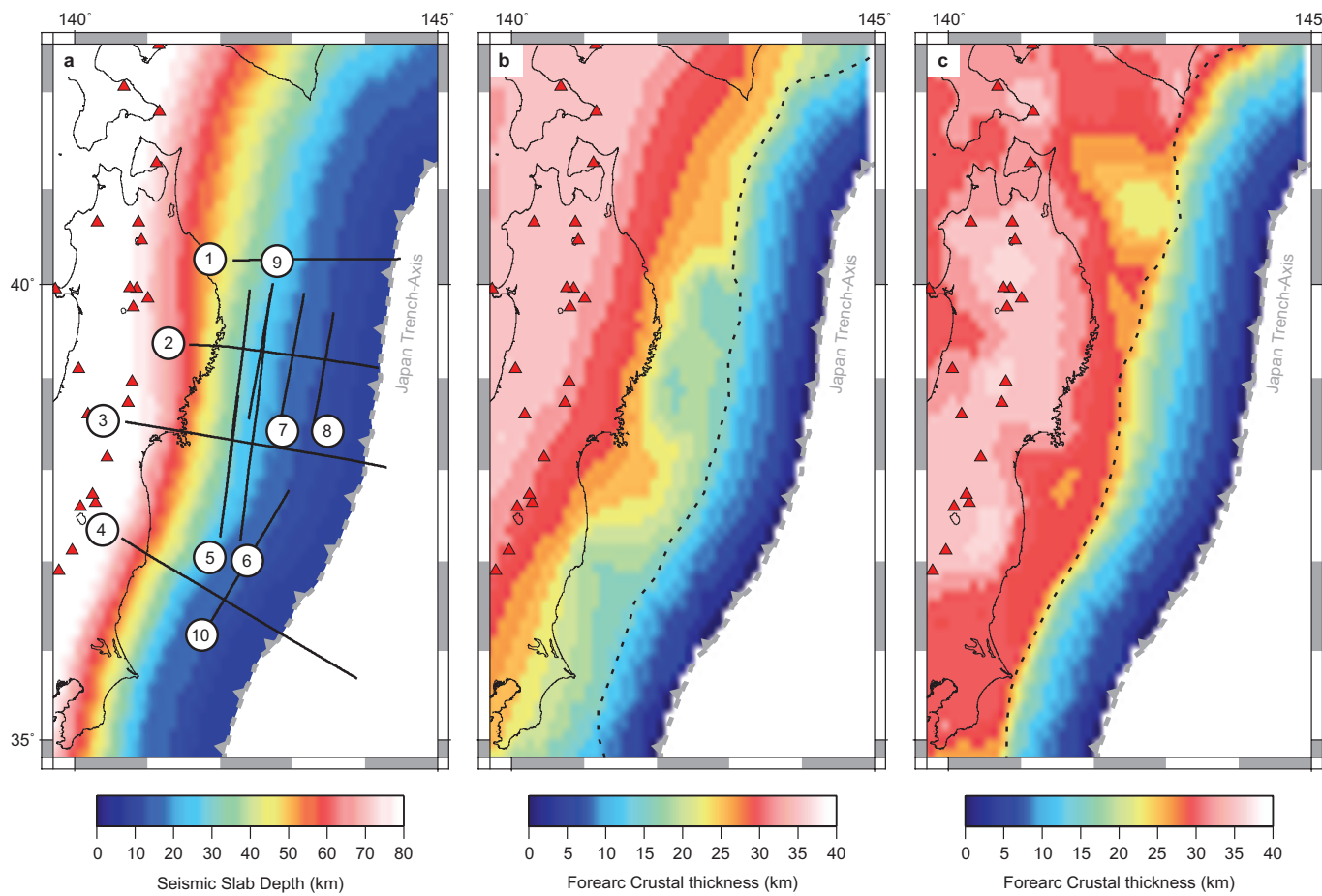
**Extended Data Figure 2 | Grid processing methodology.** Panels illustrate the ensemble-averaging and grid-processing methodology as applied at the northeast Japan subduction zone. Regional grids of bathymetry<sup>33</sup> and free-air/Bouguer-corrected (FA/BC) gravity anomaly<sup>32</sup> are sampled along trench-normal profiles (a and b). The spectral average is calculated from

each ensemble of profiles (shown as insets to c and d). Maintaining the geometry of the trench, grids of the average profile are constructed (c and d), and subtracted from the original data sets to reveal residual bathymetry (e) and residual gravity anomalies (f). This technique of spectral averaging is identical to that applied globally<sup>9,10</sup>.



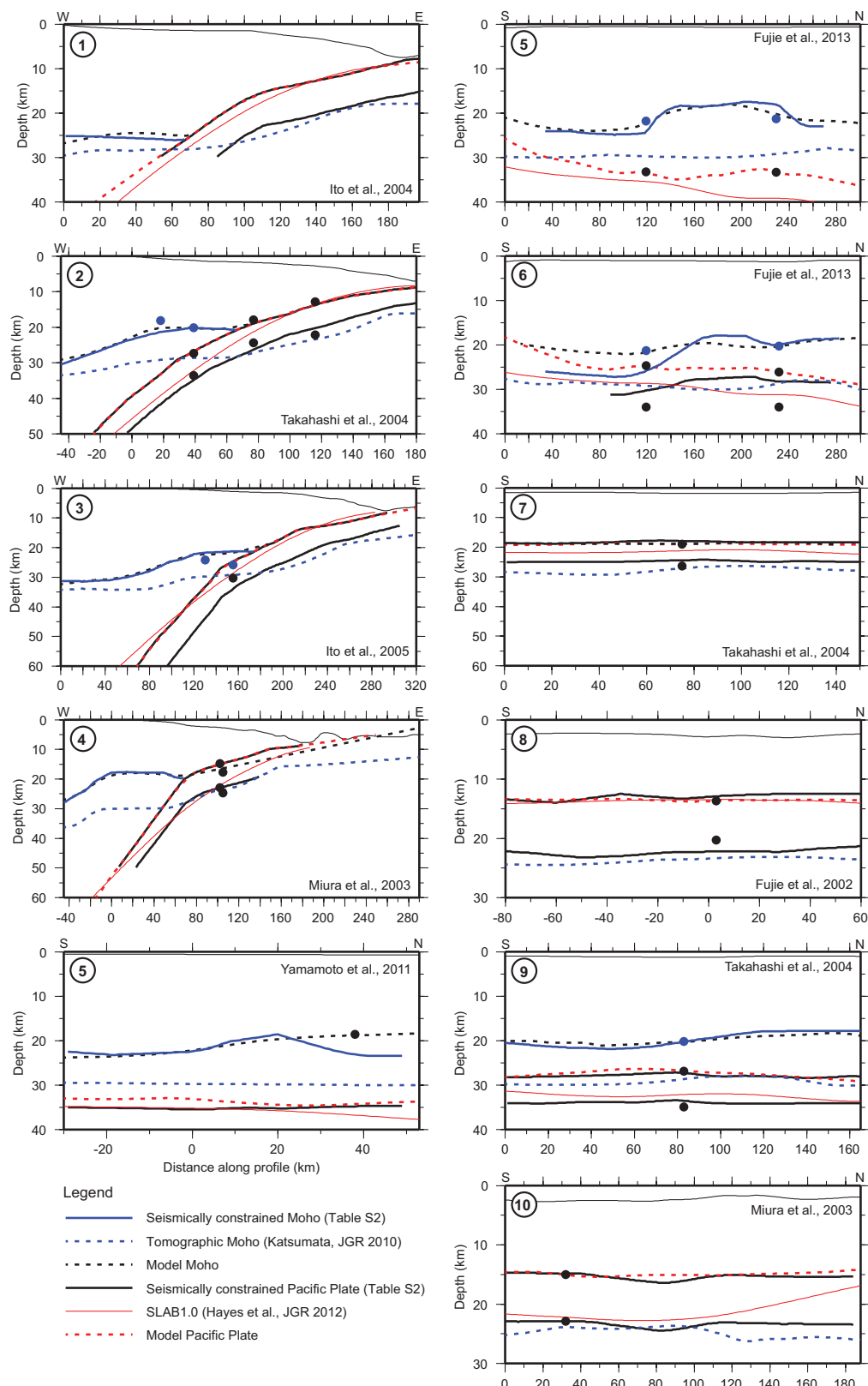
**Extended Data Figure 3 | Ensemble average profiles and two-dimensional gravity model.** **a**, Ensemble average topographic profile. **b**, Ensemble average gravimetric profile (black). The red profile shows the gravity anomaly calculated for the two-dimensional density structure shown in **d**. **c**, Mean forearc density (left) and forearc crustal thickness (right) plotted against distance from the trench axis. The larger amplitudes of density anomalies near the trench predominantly reflects the reduction in forearc crustal thickness  $h$  although they may also reflect, in part, contrasting resistances to near-trench deformation. **d**, Model of crustal structure for the northeast Japan subduction zone. This model is constructed using the mean geometry of the trench slope (shown in **a**)

and subducting slab, seismic constraints on forearc and subducting slab ( $\sim 7 \text{ km}$ ) crustal thicknesses (Supplementary Table 2), and using reasonable values for crustal ( $\sim 2,800 \text{ kg m}^{-3}$ ) and mantle densities ( $\sim 3,100 \text{ kg m}^{-3}$ ). The good fit observed in **b** between the ensemble average (black) and calculated (red) gravity anomalies shows that the ensemble average gravity anomaly captures the broad crustal architecture of the subduction zone, which enables the residual anomalies revealed following the removal of this average to be interpreted. The short-wavelength nature of residuals in the northeast Japan forearc suggests that most are related to crustal structure.

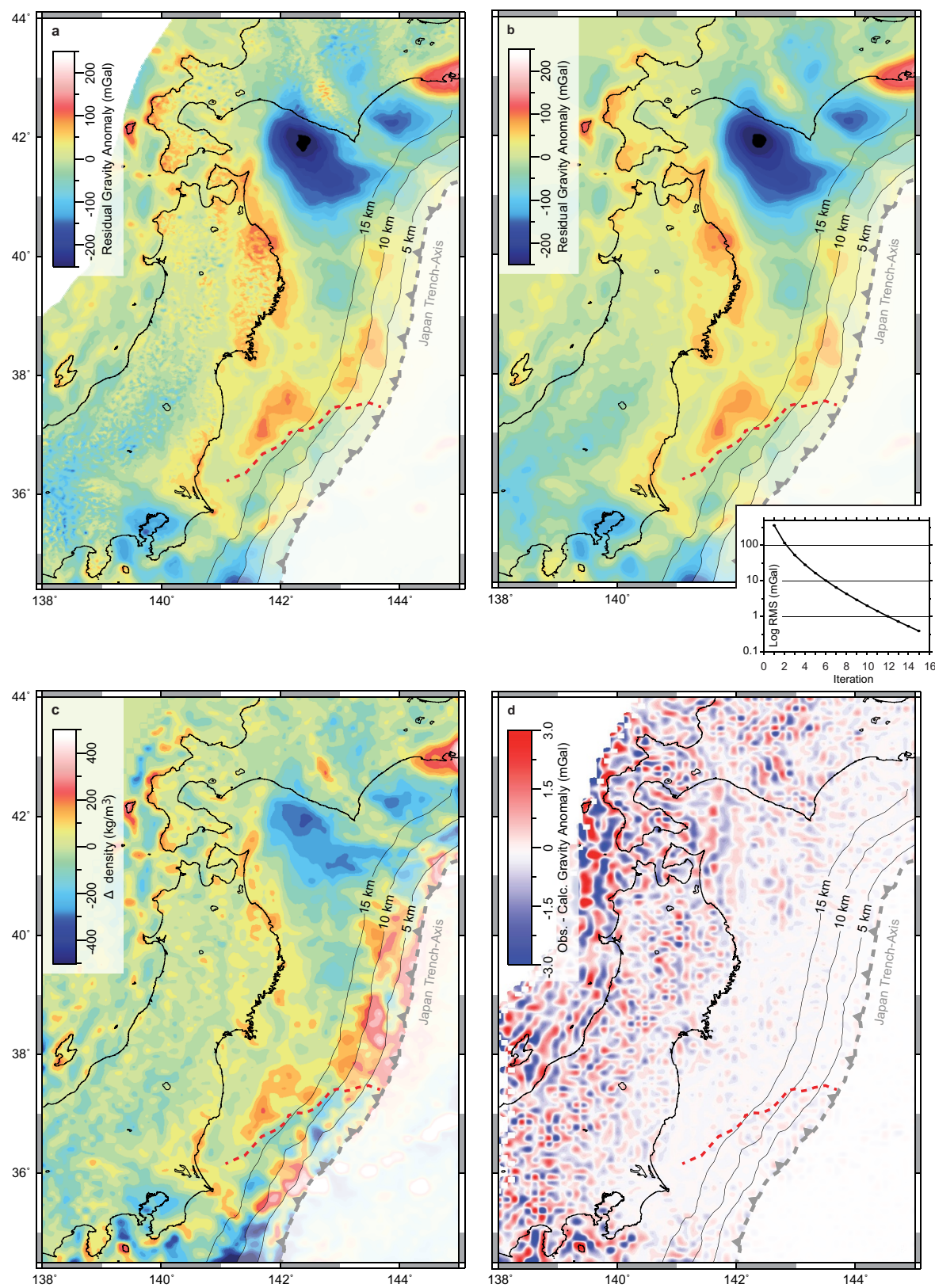


**Extended Data Figure 4 | Subducting slab geometry and forearc crustal thickness.** **a**, Geometry of the subducting Pacific Plate as constrained by linearly interpolating along-strike between active-source wide-angle seismic profiles<sup>49–56</sup>. Profiles are numbered as listed in Supplementary Table 2 and plotted in Extended Data Fig. 5. Red triangles show arc volcanoes. **b**, Forearc crustal thickness as constrained by the wide-angle

profiles shown in **a**. The dotted line marks the intersection of the subducting slab with the forearc Moho. Crustal thickness is calculated by subtracting the observed bathymetry from the seismically constrained base of the forearc crust. **c**, As in **b**, but with forearc Moho depth constrained by the tomographic model of Katsumata<sup>37</sup>.

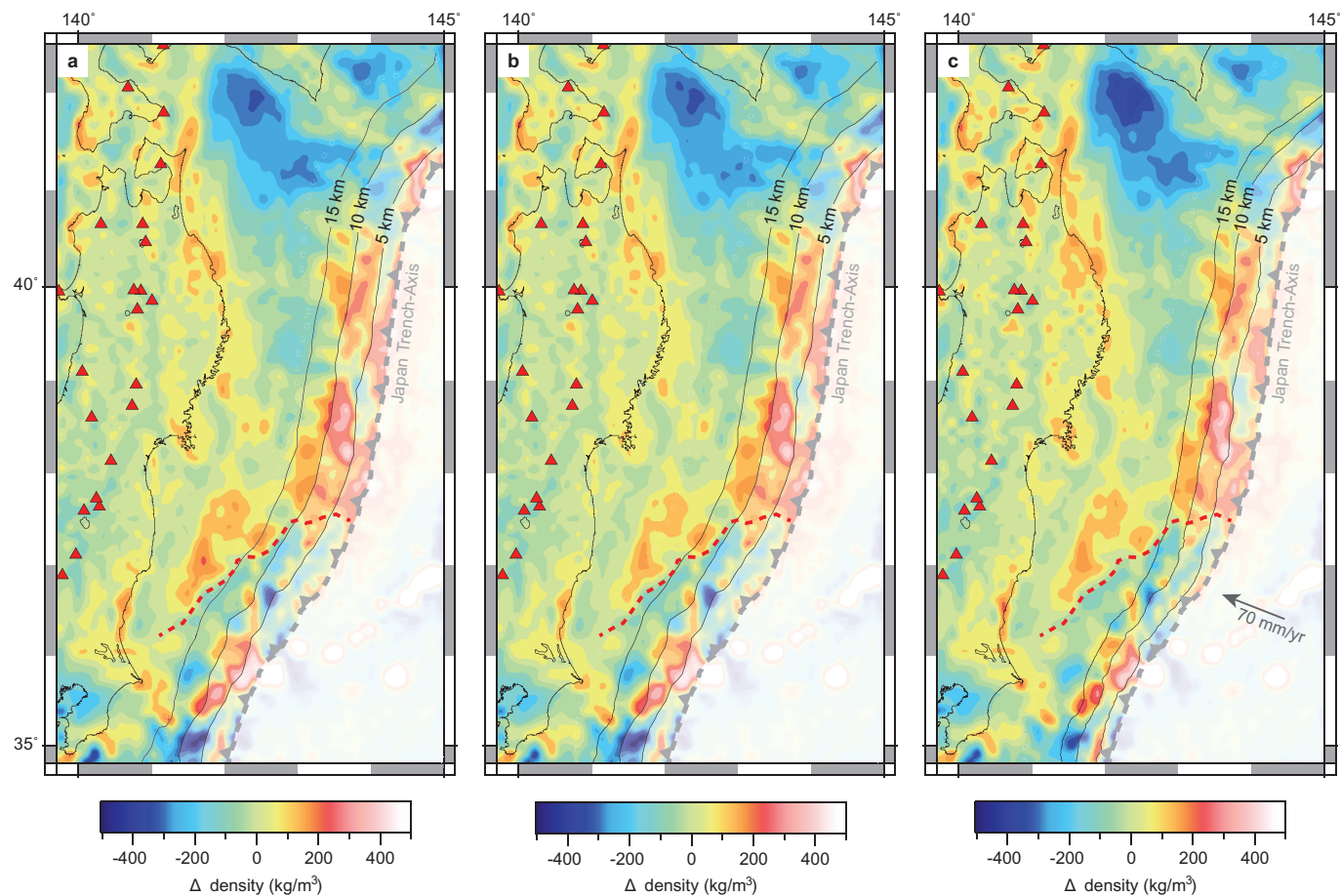


**Extended Data Figure 5 | Wide-angle seismic models.** Profiles are numbered as in Extended Data Fig. 4a and Supplementary Table 2<sup>49–56</sup>. See legend for figure nomenclature. Dots show slab and Moho positions at profile intersections. Horizontal axes show model kilometres. The slab and Moho geometries shown for profiles 5 and 6 are from reflector distributions imaged by travel-time mapping<sup>54</sup>. Intersecting profile 3 suggests that Moho reflectors interpreted south of 120 km on profile 6 may originate from the top of the subducting Pacific plate and forearc Moho constraints are only incorporated north of model kilometre 150.



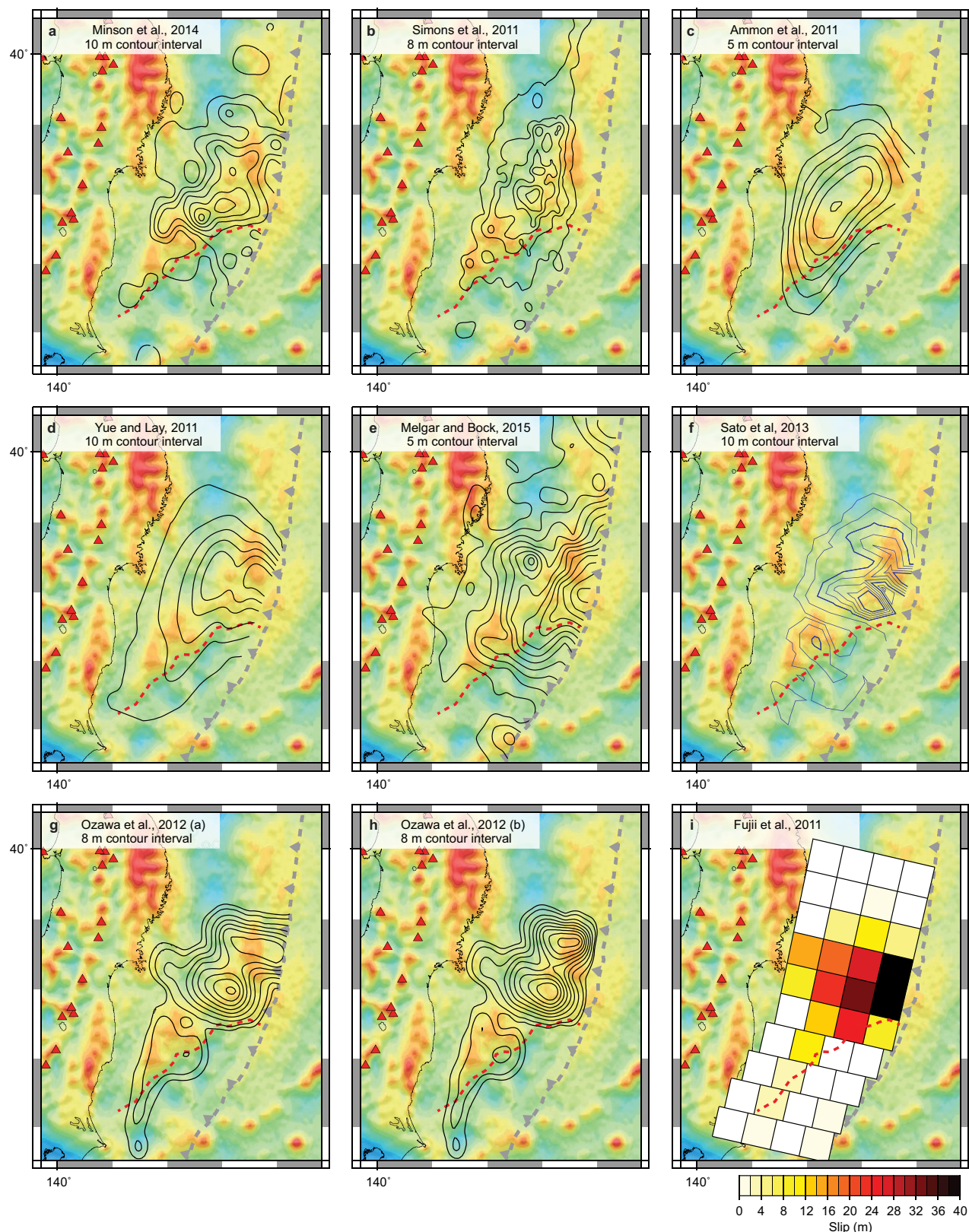
**Extended Data Figure 6 | Calculation of forearc density anomalies.**  
**a**, Observed residual gravity anomalies. Black contours show forearc crustal thickness (5 km increment). **b**, Synthetic gravity anomalies calculated from the distribution of forearc density anomalies shown in **c**. **c**, Distribution of density anomalies. Density contrasts are constant within 10 km × 10 km vertical prisms extending between the seabed and either the top of the subducting slab or the forearc Moho (whichever is

shallower). Initial density contrasts for each prism are estimated directly from residual gravity anomalies using the known thicknesses of each prism, with the difference between observed and synthetic residual gravity anomalies similarly applied to update model parameters. The inset to **b** shows the reduction in root-mean-square misfit with each update of model parameters. After 12 iterations the root-mean-square misfit < 1 mGal. **d**, Difference between observed and synthetic residual gravity anomalies.



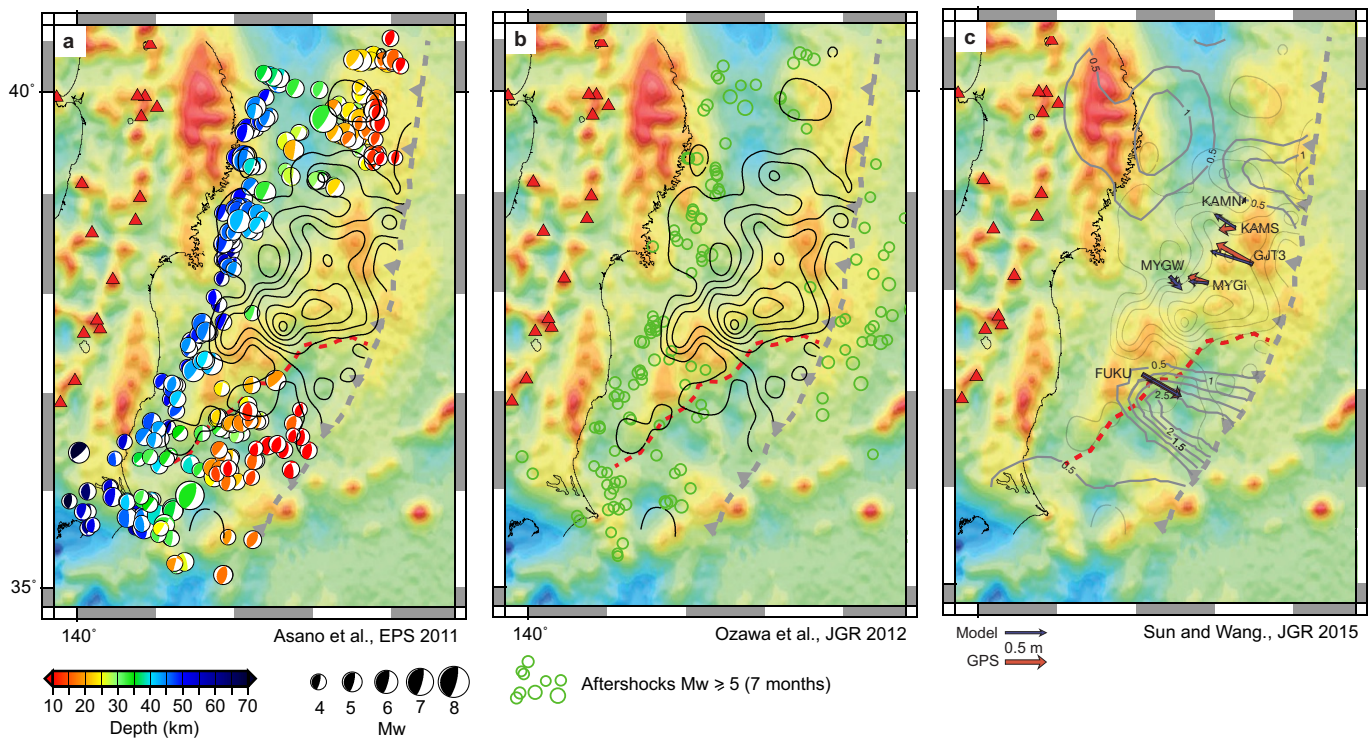
**Extended Data Figure 7 | Density anomalies calculated using different constraints on forearc crustal thickness.** **a**, Density anomalies calculated using active-source seismic constraints on the slab and forearc Moho (Extended Data Fig. 4a and b). **b**, Density anomalies calculated using active-source seismic constraints on the geometry of the subducting Pacific Plate, but using the tomographic model of Katsumata<sup>37</sup> to constrain the forearc Moho (Extended Data Fig. 4c). **c**, Density anomalies calculated using SLAB1.0<sup>36</sup> for the subducting Pacific Plate and assuming a planar forearc Moho at the mean depth (25 km) determined by active-source

seismic models. The difference in density models calculated using these different model parameterizations are of the order of  $10\text{--}20 \text{ kg m}^{-3}$ . All panels show a clear north-to-south reduction in density anomalies across the forearc segment boundary (red dashed line), and our interpretation of this contrast is not dependent on the observations used to constrain forearc crustal thickness. A comparison between forearc structure inferred from residual gravity anomalies and the seismic velocity structure of the forearc<sup>57</sup> is shown in Supplementary Fig. 1.



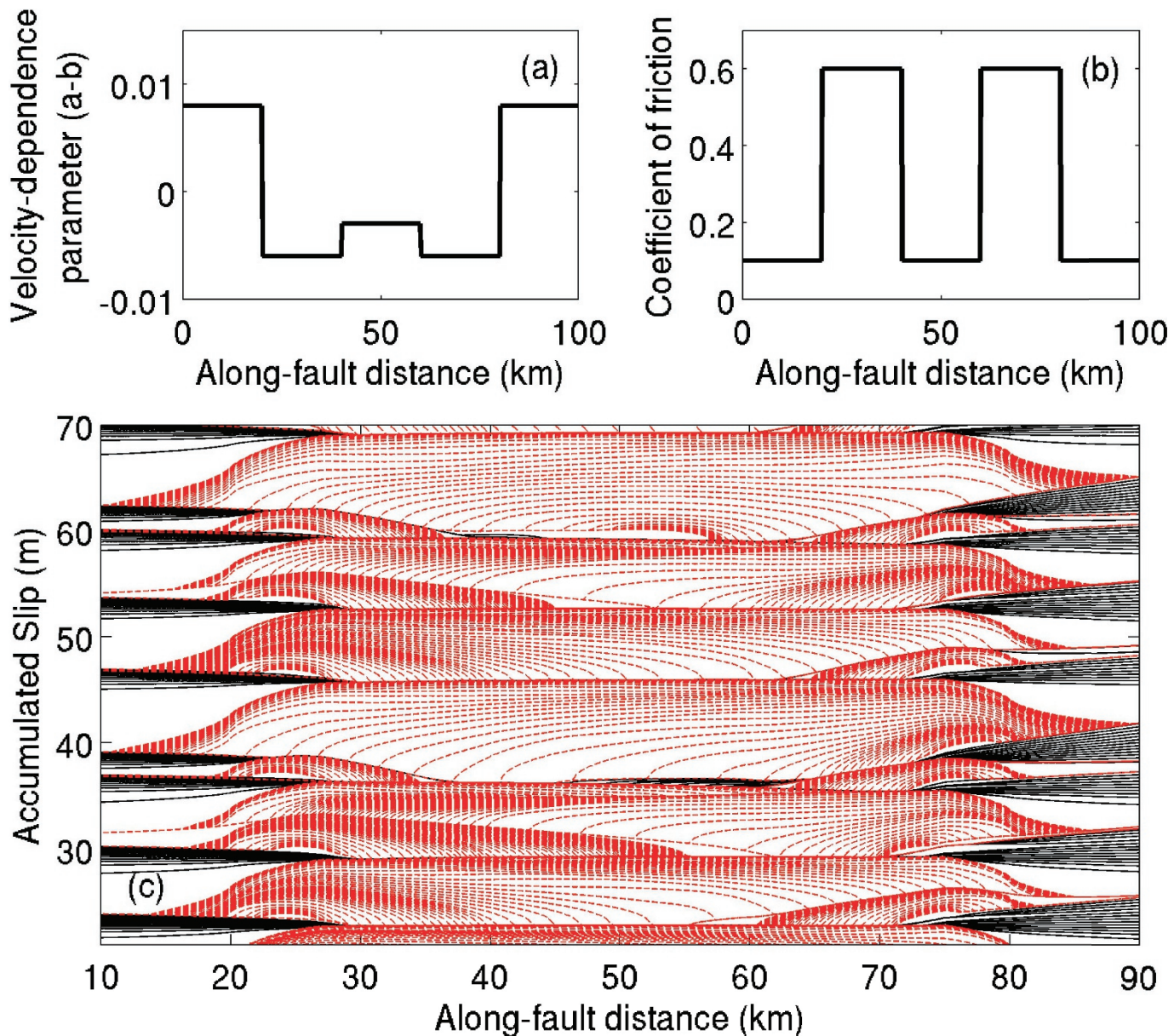
**Extended Data Figure 8 | Co-seismic slip models for the March 2011 Tohoku-oki earthquake.** Plots showing the correlation between overthrusting plate structure as constrained by residual gravity anomalies and the distribution of slip in the Tohoku-oki earthquake. These models have been constructed using different data types and inversion strategies. In all plots, grey and red dashed lines mark the trench axis and the forearc segment boundary respectively. Contour intervals are labelled and the outermost contour is 0. **a**, Minson et al.<sup>1</sup>; **b**, Simons, et al.<sup>58</sup>; **c**, Ammon et al.<sup>59</sup>; **d**, Yue and Lay<sup>60</sup>; **e**, Melgar and Bock<sup>61</sup>; **f**, Sato et al.<sup>62</sup>;

**g**, Ozawa et al.<sup>63</sup> (allowing slip at trench); **h**, Ozawa et al.<sup>63</sup> (imposing no-slip condition at trench); **i**, Fujii et al.<sup>64</sup>. In all plots, large co-seismic slip is focused north of the forearc segment boundary in regions characterized by positive residual gravity anomalies. Most models also show a sharp reduction in the magnitude of slip from north to south across the forearc segment boundary. The wide range of data types and inversion strategies represented by this ensemble of models suggests that the common features identified above are probably robust characteristics of the Tohoku-oki earthquake rupture.



**Extended Data Figure 9 | Postseismic observations.** **a**, Aftershocks between March 11 and May 24 occurring on the subduction interface<sup>65</sup>. All plots show the trench axis (grey dashed line), forearc segment boundary (red dashed line) and contours (10 m) of co-seismic slip<sup>1</sup>. **b**, All aftershocks (variable location/mechanism) occurring within seven months of the Tohoku mainshock with  $M_w \geq 5$  (ref. 63). Panels **a** and **b** show that interplate aftershocks for the Tohoku-oki earthquake did not occur in areas that experienced large co-seismic displacements. The vast majority occur in regions surrounding the mainshock rupture area, the distribution of which supports the Bayesian slip distribution of ref. 1, and provides a useful constraint on the along-strike extent of co-seismic rupture. The negative correlation between co-seismic slip and aftershock locations is strongest for the aftershock locations of ref. 65, because they have a lower magnitude cut-off (and hence more events) and because they evaluate Kagans angles to isolate interplate aftershocks from those occurring within either the subducting or overthrusting crust, both of which show no correlation with the co-seismic rupture area (see figure 3b and c of ref. 65).

These aftershock locations and the distributed slip models shown in Extended Data Fig. 8 suggest that large co-seismic displacements ( $>20$  m) in the Tohoku-oki earthquake did not continue  $>50$  km southeast of the MTL. **c**, Afterslip. Red arrows show one-year postseismic displacements of seafloor GPS sites. Blue arrows show predicted GPS vectors from the viscoelastic model of Sun and Wang<sup>24</sup>. Thick grey contours (numbers are in metres) show the distribution of afterslip<sup>24</sup>. In the dip direction, shallow afterslip is constrained to occur predominantly seaward of site FUKU and thus south of the forearc segment boundary. In the along-strike direction, the northern termination of the afterslip patch is expected to be south of the main rupture area. To the south, the afterslip may extend much farther than depicted by the slip patch shown in Extended Data Fig. 9c and may extend as far south as the Joban seamount chain<sup>24</sup>. The occurrence of rapid afterslip is exactly what would be expected if the region southeast of the forearc segment boundary displayed rate-strengthening behaviour during the Tohoku-oki earthquake.



**Extended Data Figure 10 | Numerical model of earthquake cycles on a fault obeying rate-state friction in the presence of spatially heterogeneous frictional properties.** **a,** Assumed distribution of the rate-dependence parameter  $a - b$ . **b,** Assumed distribution of the coefficient of friction. **c,** Evolution of fault slip in space and time. Black lines denote interseismic fault slip every 5 years, and red dashed lines denote coseismic slip with a time interval of 2 s. To illustrate the effects of spatial variations in the coefficient of friction and the rate-dependence parameter  $a - b$  on the patterns of seismicity, we performed simulations of earthquake cycles of a fault governed by rate-state friction. We assumed a relatively simple case of two asperities (high stress, strong velocity-weakening fault sections) separated by a weak (low coefficient of friction, weak velocity-weakening fault section). The computational domain is 100 km long, and the characteristic size of asperities is 20 km. Simulations were performed using a boundary integral method<sup>66,67</sup>. The fault is driven at a fault distance of 100 km by prescribing a constant velocity of 100 mm yr<sup>-1</sup>. We assumed a constant normal stress of 50 MPa, and slip-weakening

displacement of 10 mm. Unlike the case of a single velocity-weakening asperity that evolves to a sequence of characteristic earthquakes, the modelled earthquake sequence reveals a rich complexity and resembles many features of seismicity in the Tohoku area. There are a number of sub-events of variable size that nucleate predominantly at the boundaries of high-strength asperities, but are arrested before they grow into system-size earthquakes. These sub-events may be analogous to large ( $M_w$  7) earthquakes that occurred in the Tohoku area before and after the great 2011 earthquake. Occasionally, the entire area breaks in a mega-event (for example, between 60 m and 70 m of cumulative slip). The slip magnitude in these events is determined by the prior slip history and pre-stress. The model also predicts episodic creep in the middle of the velocity-weakening patch (for example, at 38 m of cumulative slip between 45 km and 60 km) that may be relevant to inferences of low seismic coupling of certain parts of the megathrust. Additional complexity in slip behaviour is likely to be introduced by variations in frictional properties at different spatial wavelengths, and in both along-strike and down-dip directions.